Growth of graphene-supported hollow cobalt sulfide nanocrystals via MOF-templated ligand exchange as surface-bound radical sinks for highly efficient bisphenol A degradation

Changqing Zhu[a], Fuqiang Liu[a,b,*], Chen Ling[a], Hao Jiang[a], Haide Wu[a], Aimin Li[a,b]

[a] State Key Laboratory of Pollution Control and Resources Reuse, School of the Environment, Nanjing University, Nanjing 210023, PR China
[b] State Environmental Protection Engineering Center for Organic Chemical Industrial Waste Water Disposal Resource Reuse, Nanjing 210023, PR China

ARTICLE INFO

ABSTRACT

Graphene nanosheet-supported hollow cobalt sulfide nanocrystals (Co_3S_4@GN, CoS@GN) were fabricated via a facile ligand exchange route using metal-organic frameworks (MOFs) as self-templates. Subsequent thermal annealing induced the phase transformation of Co_3S_4 to CoS. This synthesis strategy drove the cobalt ions inside zeolitic imidazolate frameworks (ZIF-67) to migrate outwards, forming a highly reactive shell composed of abundant exposed active sites to activate peroxymonosulfate (PMS) in the sulfate radical ($SO_4^{\cdot-}$)-based advanced oxidation process (SR-AOP). The graphene support exhibited excellent efficiencies in the enrichment of targeted pollutant as well as the charge transfer between absorbed molecules and radicals. The nanocatalysts were fully characterized and applied to the catalytic degradation of bisphenol A (BPA). Benefitting from the unique structure characteristic, the as-synthesized nanocomposites showed superior catalytic activities over a broad pH range. The degradation efficiency of BPA reached ~100% within 8 min by using CoS@GN, and the kinetic constant (0.62 min^{-1}) was higher than those of most reported heterogeneous catalysts by 1–2 orders of magnitude. Furthermore, the critical roles of graphene support in regulating the variety and action site of radicals were addressed for the first time. The adsorptive and conductive graphene made the $SO_4^{\cdot-}$ once produced was consumed immediately, which limited the diffusion of $SO_4^{\cdot-}$ out of catalyst surface and the generation of $\cdot OH$. The catalyst served as a surface-bound $SO_4^{\cdot-}$ sink for the in-situ degradation of adsorbed BPA. Catalyst characterizations and the Density-Functional-Theory (DFT) calculation confirmed the excellent activity of CoS@GN in yielding $SO_4^{\cdot-}$ with Co(II) as the active center. A CoS@GN-coated membrane reactor was constructed to avoid catalyst loss and worked well in consecutive 3 cycles, suggesting the satisfactory catalyst reusability and system robustness. Overall, this work paved a new way for MOFs in the environmental application and provided a novel family of Co-based nanocatalysts to produce surface-bound radicals for recalcitrant contaminant degradation by SR-AOP.

1. Introduction

Nowadays, the ever-growing water contamination originated from uncontrolled industrial emission has attracted a great deal of public concern. Especially, the endocrine disrupting chemicals (EDCs) are deemed as emerging pollutants with significant estrogenicity and persistence, which adversely interfere with the quality of human life through food chains and environmental cycles [1]. Bisphenol A (BPA) as a representative EDCs is widely used in the manufacture of plastics and ubiquitously distributed in the aquatic environment [2,3]. Development of efficient methods to remove BPA is highly urgent and challenging. Among all approaches, the sulfate radical ($SO_4^{\cdot-}$)-based advanced oxidation process (SR-AOP) is a powerful technology in terms of full decomposition of recalcitrant pollutants by creating highly reactive $SO_4^{\cdot-}$ [4–6]. Compared with hydroxyl radical ($\cdot OH$), $SO_4^{\cdot-}$ exhibits inherent advantages of higher reduction potential (2.5–3.1 V *vs* 1.8–2.7 V), wider pH adaptability and longer lifetime ($t_{1/2}$ = 30–40 μs *vs* 10^{-3} μs) [7]. $SO_4^{\cdot-}$ can be produced by coupling transition metal ions with peroxymonosulfate (PMS), and cobalt ion (Co^{2+}) has proved to be the best activator [8]. While considering the disadvantages of homogeneous process associated with the generation of secondary pollution and the difficulty in catalyst recycling, researchers deflect to develop

heterogeneous cobalt-based catalysts [9,10]. However, the current popular catalysts were almost limited to cobalt or cobalt-containing oxides, and the kinetic activity (first-order kinetic constant, $k = 10^{-3}$- 10^{-1} min^{-1}) is far from satisfactory for practical application in BPA degradation [11–14]. The innovation of new class of cobalt-based catalysts for PMS activation possibly breaks new ground for the further improvement of catalytic efficiency.

The cobalt sulfides (CoS_2, Co_3S_4, CoS, Co_9S_8, etc.) represent a significant class of semiconductors and have gained increasing interest in lithium ion batteries, water-splitting electrocatalysts and supercapacitors [15–19]. The high performance of cobalt sulfides in these fields hints the potential in SR-AOP for PMS activation, which has been rarely explored to date. Although vast cobalt sulfides with delicately controlled composition and morphology were constructed [20,21], the design of novel effective catalysts suitable for BPA degradation is still a challenge. Increasing the number of exposed surface active sites and enhancing the electrical conductivity are effective ways to improve the catalytic activity. Metal–organic frameworks (MOFs) are the supramolecular assemblies of metal ions with organic ligands, and are characterized by diverse skeletons and well-defined pore structures [22,23]. Recently, the cobalt-rich zeolitic imidazolate framework (ZIF-67) was used as a sacrificial template to construct the hollow Co_3S_4 nanobox for hydrogen evolution reactions [24]. The formation of hollow Co_3S_4 was ascribed to the Kirkendall effect originated from the different diffusion rates of cobalt and sulfur species. This strategy drove the cobalt ions inside ZIF-67 to migrate outwards, forming a highly reactive shell composed of dense ultrafine Co_3S_4 nanocrystals. As an improvement, Chen reported an interlaced carbon nanotubes (CNTs) threaded hollow Co_3S_4 hybrid catalyst [18]. The three-dimensional conductive CNTs network facilitated the electron transport to promote redox reactions all-over the electrode. However, as far as we know, there are few reports of MOFs-derived cobalt sulfide nanostructures for PMS activation in environmental applications and the activation process requires to be well illustrated.

Herein, we synthesized novel graphene-supported cobalt sulfide nanocatalysts via a MOF-templated ligand exchange route. Graphene nanosheet was used as the support because it could (i) suppress excessive MOF assembly and provide nucleate sites to grow highly-dispersive cobalt sulfide nanocrystals [25,26]; (ii) offer adsorption domains for the enrichment of BPA from bulk solution through π-π interaction, leading to a high local concentration of reactants [27]; (iii) guarantee the fast electron transport between adsorbed BPA molecules and $SO_4^{\cdot-}$ to enhance the redox rate [28]. The as-prepared nanocomposite exhibited attractive catalytic activity in SR-AOP for BPA degradation, and a kinetic rate constant of 1–2 orders of magnitude higher than those of most reported catalysts was realized. More importantly, after being supported on the conductive and adsorptive graphene matrix, the cobalt sulfide nanocatalyst served as a unique radical sink where high instantaneous concentration of $SO_4^{\cdot-}$ once produced was confined on the surface microenvironment rather than diffused into the bulk solution, which provided another driving force to facilitate the oxidation degradation of BPA. This was the first time to address the effect of support on the action site of metal-produced radicals in SR-AOP. With the systematic evaluation on BPA degradation, and the mechanism exploration through catalyst characterizations and the Density-Functional-Theory (DFT) calculation, we demonstrated cobalt sulfides hold great promise as PMS activators for pollutant remediation.

2. Experimental and theoretical methods

2.1. Chemicals and materials

Graphite powder was purchased from American Bay Carbon (Bay City, MI). Bisphenol A (BPA), oxone® ($2KHSO_5 \cdot KHSO_4 \cdot K_2SO_4$, as PMS source), cobalt nitrate hexahydrate ($Co(NO_3)_2 \cdot 6H_2O$, 99%), thioacetamide (CH_3CSNH_2), absolute ethanol, methanol and 2-methylimidazole (2-MIM, 99%) were bought from Sinopharm Chemical Reagent Co., Ltd. (China). All chemicals were used as received without further purification. Ultrapure water from the Milli-Q Plus system (Millipore, Bedford, USA) was used to prepare stock solutions.

2.2. Catalyst preparation

2.2.1. Preparation of ZIF-67@GN

Graphene oxide (GO) was prepared according to a modified Hummers method (Details in SI Text S1). Then, 10–60 mg GO was fully dispersed in 25 mL water under sonication for 30 min. Subsequently, 240 mg $Co(NO_3)_2 \cdot 6H_2O$ was dissolved in the GO solution and magnetically stirred for 1 h. Afterwards, 40 mL aqueous solution of 1.092 mol/ L 2-MIM was rapidly added to the above mixture under stirring. After being stirred for 15 min, the precipitate was collected by centrifugation, rinsed several times with water, and dried under vacuum at 70 °C for 12 h. The obtained product was termed as ZIF-67@GN-x (x = 10–60 in accordance to the GO weight). The pristine ZIF-67 was also prepared using the same procedure but without adding GO.

2.2.2. Preparation of Co$_3$S$_4$@GN

Briefly, 60 mg ZIF-67@GN-x (x = 10–60) and 90 mg thioacetamide (TAA) were dispersed into 30 mL ethanol under sonication to form a uniform suspension. The mixture was transferred into a 50 mL Teflon-line sealed autoclave and heated at 120 °C for 4 h. The product was collected by centrifugation, washed thoroughly with ethanol for several times, and finally dried at 70 °C for 12 h under vacuum. The obtained product was named as Co_3S_4@GN-x (x = 10–60 in accordance to the GO weight). Similarly, Co_3S_4 was prepared by using ZIF-67 as the precursor instead of ZIF-67@GN.

2.2.3. Preparation of CoS@GN by phase transformation

The CoS@GN was synthesized through the heat-induced phase transformation of Co_3S_4@GN. Generally, the porcelain boat with Co_3S_4@GN-x (x = 10–60) was put into a tube furnace for calcination at 600 °C for 2 h at a heating rate of 10 °C /min under N_2 flow and then cooled down to room temperature. The formed product was termed as CoS@GN-x (x = 10–60 in accordance to the GO weight). Similarly, CoS was prepared by using Co_3S_4 as the precursor.

2.3. Characterizations

Field-emission Scanning electron microscopy (FE-SEM) images were obtained by a Hitachi S-4800 instrument equipped with an accessory EDX spectrometer at an accelerating voltage of 5 kV. Transmission electron microscopy (TEM), scanning transmission electron microscopy (STEM) and elemental mapping analysis were performed using a JEOL JEM-2100 F microscope operated at 200 kV. X-ray diffraction (XRD) patterns were collected on a Rigaku RINT 2000 X-ray diffractometer with monochromatic Cu Kα radiation (40 kV, 40 mA) at a scanning rate of 1°/min. Thermogravimetric analysis (TGA) data were collected with a NETZSCH-STA-449C thermal balance in N_2 atmosphere with a heating rate of 10 °C/min. N_2 adsorption/desorption isotherms were recorded at −196 °C using a Quantachrome Autosorb-IQ-2C analyzer. The surface area was determined by the Brunauer—Emmett—Teller (BET) method, and the pore size distribution was analyzed by the nonlocal density functional theory (NLDFT) and Barrett-Joyner-Halenda (BJH) methods. Fourier transform infrared (FT-IR) spectra were measured on a Bruker VERTEX 70 IR spectrometer. Raman spectra were recorded on a Thermo Fisher DXR Raman spectrometer employing a 532 nm laser. X-ray photoelectron spectroscopy (XPS) spectra were obtained by using a PHI Quantera SXM (ULVAC-PHI) instrument with an Al Kα X-ray source. All binding energies were calibrated via referencing C 1 s binding energy (285.0 eV). The acid-base surface chemistry of the catalyst was investigated through the potentiometric titration

using an automatic titration system (T50, Mettler Toledo) with a combined glass electrode (DGi115-SC) (Details in SI Text S2). The electrochemical impedance spectrum (EIS) measurements were conducted on a CHI 660 B electrochemical system (Shanghai, China) in a typical three-electrode setup with an electrolyte solution of Na_2SO_4 (0.1 mol/L). A Pt plate and a saturated calomel electrode (SCE) were used as the counter electrode and reference electrode, respectively. A glassy-carbon electrode with a diameter of 3 mm covered by a thin catalyst film was used as the working electrode. Typically, 2 mg catalyst was suspended in 1 mL ethanol to form a homogeneous ink assisted by ultrasound for 10 min. Then, 0.8 mL of the ink was spread onto the surface of glassy-carbon electrode by a micropipette and dried under room temperature for use.

2.4. Catalytic degradation procedure

Unless otherwise specified, all of the degradation experiments were carried out in a 100 mL reactor containing 50 mL of BPA solution (20 mg/L) at room temperature (25 °C). The pH was adjusted by dilute sodium hydroxide or sulfuric acid solution. Typically, 5 mg catalyst was added into the BPA solution. After 1 min ultrasonic dispersion, a uniform suspension was created, which was then stirred for 30 min to establish the adsorption-desorption equilibrium. Then, 0.5 mL of 20 mg/mL oxone solution was added to the suspension (PMS: 0.1 g/L) to initiate the reaction. 0.5 mL of the suspension was withdrawn and quenched with 0.5 mL methanol at given time intervals. Afterwards, the sample was filtered through a 0.22 um polytetrafluoroethylene (PTFE) filter into a high-performance liquid chromatography (HPLC) vial for subsequent BPA concentration measurement. For the construction of CoS@GN-60-coated membrane reactor, a 5 mL suspension containing well-dispersed CoS@GN-60 catalyst (0.5 mg) was filtrated through the above PTFE film. Then, two membrane reactors were connected to get a two-grade reactor system for treating the flow-through BPA solution.

2.5. Analytic methods

The BPA concentration was analyzed on a HPLC system (Agilent 1200 infinity series) equipped with a G1315D 12,600 DAD detector and a C18 column. A methanol/water (70:30, v/v) mixture was used as the mobile phase at a flow rate of 1.0 mL/min, and the detection wavelength was 230 nm. The intermediate products of BPA degradation were determined by a gas chromatography-mass spectrometer (GC–MS) with an Agilent 7890B GC system in combination with an Agilent 5977B single quadrupole mass spectrometric detector (Details in SI Text S3). Total organic carbon (TOC) was assayed on a TOC analyzer (Elementar,

Germany). The electron paramagnetic resonance (EPR) measurement was carried out on a Bruker ELEXSYS 580 spectrometer to detect free radicals during the PMS activation using 5,5-dimethyl-1-pyrroline N-oxide (DMPO, 98%, Adams Reagent Co., Ltd.) as the spin-trapping agent. The concentration of leached cobalt ions was measured using an inductively coupled plasma atomic emission spectrometry (iCAP 8000, USA). The BPA degradation kinetic data were fitted by the first-order kinetic model and the apparent rate constant (k) was calculated according to Eq. (1):

$$\ln \frac{C_t}{C_0} = -kt \tag{1}$$

where C_t was the BPA concentration at a certain reaction time (t) and C_0 was the initial BPA concentration.

2.6. Computational models and methodology

The spin-unrestricted density functional theory (DFT) calculation was performed using the Dmol^3 package. Exchange correlation functions were taken as the generalized gradient approximation (GGA) with Perdew Burke Ernzerhof (PBE). Double numerical plus polarization (DNP) was employed as the basis set while the all electron core treatment was utilized to include relativistic effects. The convergence tolerance of energy of 10^{-5} Hartree was applied (1 hartree = 27.21 eV), and the maximal allowed force and displacement were 0.002 hartree/Å and 0.005 Å, respectively. In the calculation, the (100) crystal face of CoS was used as the representative face for simplification and all the atoms were allowed to relax. The k points for PMS, CoS and PMS + CoS systems were set as 1*1*1, 3*3*1 and 3*3*1, respectively. To avoid the interaction of surfaces in different supercells along C direction, a 20 Å vacuum layer above the surface was constructed. The DFT-D method within the Grimme scheme was used in the calculation to take the van der waals force into account.

3. Results and discussion

3.1. Synthesis and characterization

As schematically illustrated in Fig. 1, the graphene-supported cobalt sulfide nanocatalysts were prepared with ZIF-67@GN as the precursor via a facile self-templated ligand exchange strategy. Firstly, electronegative carboxylic groups on GO nanosheet served as nucleation centers for growing uniform MOFs to obtain the ZIF-67@GN precursor. Afterwards, ZIF-67@GN was chemically converted to hollow-Co_3S_4@GN hybrid structure through a solvothermal reaction where S^{2-} derived from TAA decomposition displaced 2-MIM as the ligand. The
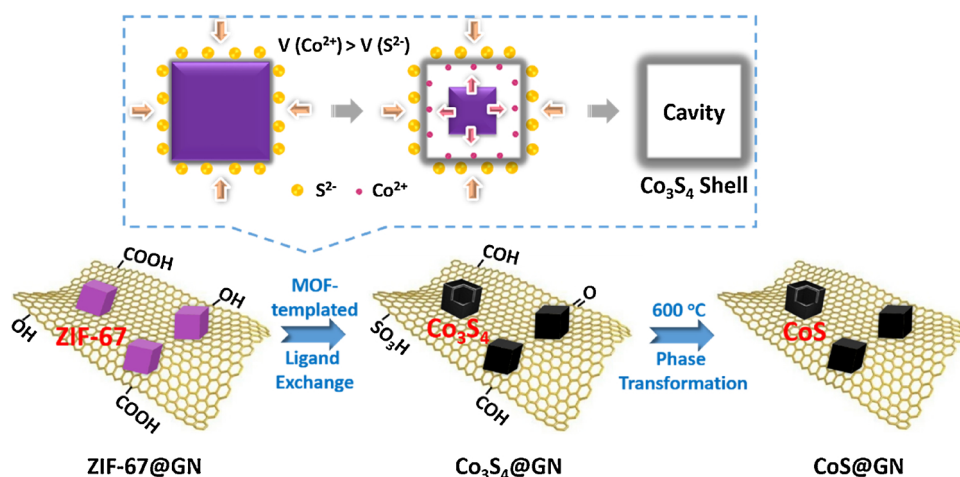

Fig. 1. Schematic diagram for the synthetic route of graphene-supported hollow cobalt sulfide nanocrystals.
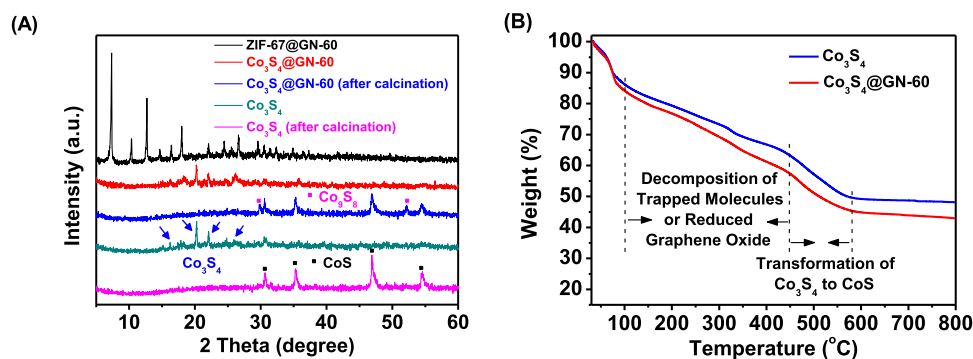
(A)

(B)

Fig. 2. (A) XRD patterns of ZIF-67@GN-60, Co_3S_4@GN-60 samples before and after calcination, pristine Co_3S_4 samples before and after calcination. (B) TGA curves of pristine Co_3S_4 and Co_3S_4@GN-60.

formation of hollow Co_3S_4 was attributed to the Kirkendall effect [24]. In detail, at the early stage, S^{2-} quickly reacted with Co^{2+} on ZIF-67 surface to form a thin layer of cobalt sulfides, which acted as a physical barrier to prevent the direct contact and chemical reaction between external S^{2-} and internal Co^{2+}. Due to the smaller ionic radius of Co^{2+} (~74 pm) than S^{2-} (184 pm), the outward diffusion of Co^{2+} through the thin shell was more easy than the inward migration of S^{2-}. Therefore, the internal MOF was gradually dissolved, and the released Co^{2+} penetrated the preformed shell to continuously react with external S^{2-}, resulting in the formation of a hollow Co_3S_4 structure. Finally, the Co_3S_4@GN products were collected and annealed in a N_2 atmosphere to induce the phase transformation of Co_3S_4 to CoS to form CoS@GN. During the synthetic process, GO was ceaselessly reduced. The photographs of ZIF-67, ZIF-67@GN, Co_3S_4@GN and CoS@GN were exhibited in SI Figure S1 for visual comparison. The XRD patterns in Fig. 2A depicted the crystal evolution in the fabrication of catalysts. For ZIF-67@GN, all diffraction peaks with strong intensities matched well with those of simulated ZIF-67, indicating the well growth of supported ZIF-67 with high crystallinity [29]. The (002) reflection peak of graphitic carbon was not obvious, possibly because of the disordered graphene structure [20]. After solvothermal sulfuration, the peaks of ZIF-67 totally disappeared while four main diffraction peaks at 16.2°, 20.2°, 22.1° and 26.1° corresponding to the (111), (200), (211) and (220) lattice planes of Co_3S_4 appeared [30]. Upon further thermal annealing, these Co_3S_4 peaks turned insignificant and the characteristic (100), (101), (102) and (110) peaks located at 30.7°, 35.4°, 46.9° and 54.5° could be readily indexed to the standard CoS (PDF 65–3418) [26]. The formation of secondary phase of Co_9S_8 was also noted, which was evident from the appearance of reflections at 2θ values of 29.8° and 52.2° [24,31,32]. For comparison, pristine Co_3S_4 and CoS in the absence of graphene nanosheet were also prepared as control samples. Similar phase transformation was observed, but pristine CoS showed higher crystalline purity without the existence of Co_9S_8, which indicated the graphene support might affect the growth and evolution of cobalt sulfide nanocrystal. TGA was also performed under a N_2 atmosphere to understand the decomposition and associated phase transition process of Co_3S_4 and Co_3S_4@GN (Fig. 2B). The first weight loss below 100 °C was ascribed to the evaporation of adsorbed water. The second loss stage of pristine Co_3S_4 at 100–450 °C should stem from the liberation or pyrolysis of organic contents, i.e., 2-MIM, TAA and its decomposition products trapped in inner cavities [32]. For Co_3S_4@GN, the second weight loss was distinctly higher due to the simultaneous thermal decomposition of labile functional groups on graphene nanosheet [33]. A third weight loss occurred at 450–580 °C, confirming the de-sulfurization of Co_3S_4 to form CoS as Eq. (2) [31].

$$Co_3S_4 \xrightarrow{Heat} 3CoS + S\uparrow \tag{2}$$

The morphological features of as-synthesized catalysts were characterized by FE-SEM and TEM. As shown in Fig. 3A, the ZIF-67 nanoparticles were well dispersed on wrinkled GO nanosheets. The poor electrical conductivity of ZIF-67 possibly led to its low recognizability under electron imaging. After solvothermal reaction, numerous Co_3S_4 nanocrystals were formed by MOF-templated ligand exchange and supported in the flexible RGO sheets (Fig. 3B). Thermal annealing did not significantly change the architecture, and CoS nanocrystals were uniformly anchored on graphene surface without evident aggregation after phase transformation (Fig. 3C). Interestingly, as shown in Fig. 3D, the pristine CoS which was prepared in the absence of GO exhibited a well-defined box-like superstructure with a size scale of 1–2 μm. Meanwhile, the hollow structure feature could be discerned unambiguously from the cracked corner with the rough shell built by dense ultrafine CoS nanocrystals. As previous studies, the distinct morphology and size change from micro-box to nanoparticle should be attributed to the presence of GO support [20,25], which hinders the excessive assembly of ZIF-67 by interface interaction. Energy-dispersive X-ray spectra (EDX, SI Figure S2) revealed Co/S atomic ratios of 0.78 in Co_3S_4@GN, and 1.10 in CoS@GN samples, consistent with the stoichiometric ratios of Co_3S_4 and CoS, respectively. The TEM image of CoS@GN (Fig. 3E) verified that a great number of nanocrystals with the size around 10–40 nm were anchored on an unfolded graphene nanosheet. A part of these CoS nanoparticles showed obvious hollow structure and well-defined inner cavity which was clearly elucidated by the sharp contrast between the center and the edge. The solid-like characteristic of certain CoS nanoparticles was considered to originate from the fact that the nanoscale crystal was too small to provide enough room for the relative diffusion of Co^{2+} and S^{2-}, and as a result, the hollow structure seemed unconspicuous. The high resolution TEM image provided further insight into the microstructure (Fig. 3F and G). The visible lattice fringes with interplanar spacings of 0.19, 0.29 and 0.25 nm were consistent with the d-spacing of (102), (100) and (101) crystal planes of CoS, respectively [20,21,25]. These results agreed well with the above XRD patterns. The cross section of few-layer graphene was also observed, indicating that the CoS nanocrystals were in tight contact with graphene surface. The element mapping analysis of CoS@GN (Fig. 3H) revealed that the composite consisted of evenly dispersed C, S and Co elements, which well matched the shape of the selected mapping area.

The FT-IR spectroscopy was carried out to identify the components of the nanocomposites (Fig. 4A). For ZIF-67@GN, the characteristic peaks in the range of 600-1500 cm^{-1} were assigned to the stretching and bending vibrations of the imidazole ring. Additionally, the peak at 1576 cm^{-1} was associated with the stretching mode of C=N bond in 2-MIM [34]. Moreover, the deformation vibration peak of O—H in GO was observed at 1418 cm^{-1} [27], demonstrating the hybridization of MOFs and GO in ZIF-67@GN. After solvothermal treatment, the peaks for 2-MIM ligand and O—H group of GO weakened significantly in intensity, which indicated the concurrent occurrence of ligand exchange and GO
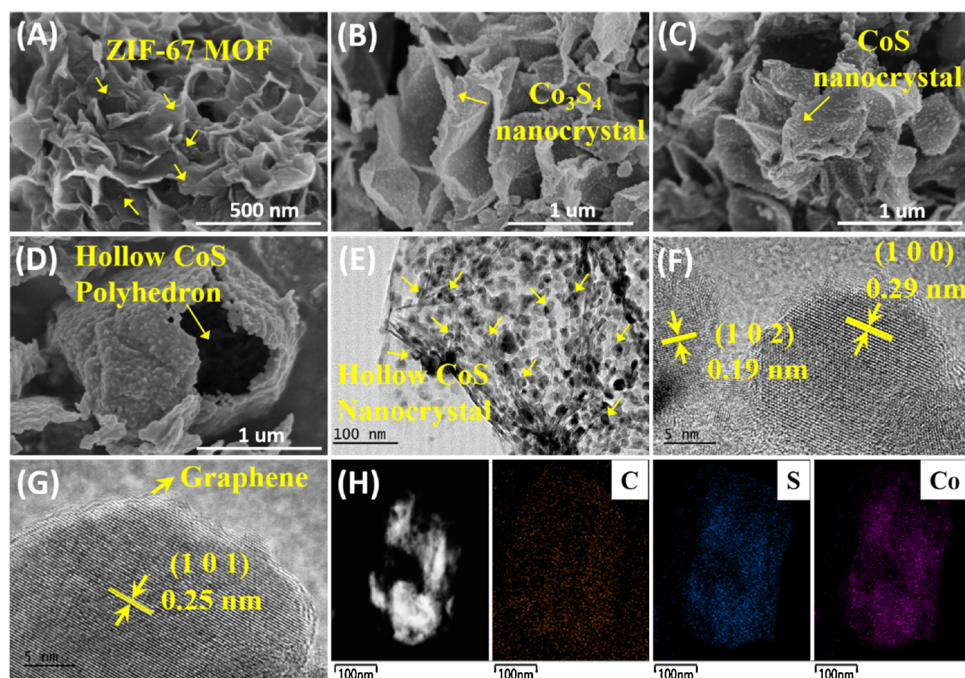
Fig. 3. SEM images of (A) ZIF-67@GN-60, (B) Co$_3$S$_4$@GN-60, (C) CoS@GN-60 and (D) pristine CoS. (E) TEM image of CoS@GN-60. (F, G) HRTEM of CoS@GN-60. (H) STEM image of CoS@GN-60 and corresponding elemental (C, S, Co) mapping images.

reduction. The oxygen-containing groups of GO was exhaustively removed by subsequent thermal annealing as the FT-IR spectrum of CoS@GN became a line in shape. The elimination of surface polar groups could improve both the hydrophobicity and conductivity of graphene, which was conducive to the BPA adsorption by hydrophobic or π-π interaction as well as the fast electron transfer. Raman spectroscopy is usually used to investigate the structural characteristic of carbon materials. All the three samples exhibited typical D band at 1352 cm^{-1} and G band at 1592 cm^{-1}, respectively (Fig. 4B). The D

band is a signature for structural defects on graphitic planes while the G band is assigned to the E$_{2g}$ vibrational mode in the sp^2 bonded graphitic carbons. The intensity ratio of D and G bands (I$_D$/I$_G$) is often employed to estimate the amount of defects on carbon materials [33]. The I$_D$/I$_G$ value increased from 1.08 for ZIF-67@GN to 1.19 for Co$_3$S$_4$@GN after solvothermal reaction, due to the decreased average size of the sp^2 domains as well as the doping of S heteroatoms [27,35]. After thermal annealing, I$_D$/I$_G$ decreased to 1.12, suggesting a restoration of the conjugation structure in graphene. Furthermore, the peak observed in
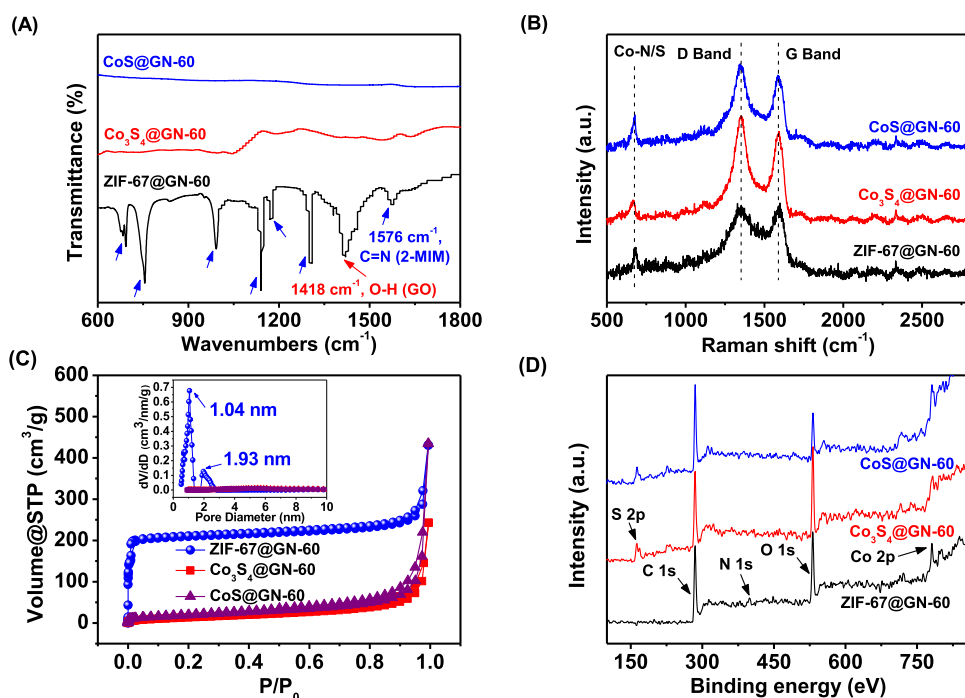

Fig. 4. (A) FT-IR spectra, (B) Raman spectra, (C) N$_2$ adsorption-desorption isotherm curves and pore size distributions (inner image) and (D) XPS wide scan surveys of ZIF-67@GN-60, Co$_3$S$_4$@GN-60 and CoS@GN-60 samples.

the lower Raman shift region of 675 cm^{-1} was assigned to the cobalt-ligand bonds [29]. Fig. 4C and Table S1 showed the N$_2$ adsorption-desorption isotherm and pore size distribution of obtained samples. The ZIF-67@GN precursor possessed a high BET surface area of 875 m^2/g, and abundant micropores with a micropore volume of 0.29 cm^3/g and a double-humped micropore diameter distribution concentrated at 1.04 nm and 1.93 nm, respectively. The ligand-exchange reaction triggered the decomposition of ZIF-67, resulting in the complete loss of micropores. Therefore, the Co$_3$S$_4$@GN presented a decreased BET surface area of 56 m^2/g with a total pore volume of 0.38 cm^3/g and average pore diameter of 27 nm. The mesoporous structure was considered to stem from the interspaces between cumulate graphene nanosheets. After calcination, the BET surface area, total pore volume and average pore diameter of CoS@GN increased to 75 m^2/g, 0.67 cm^3/g and 36 nm, respectively. It's attributed to the shrink and wrinkling of graphene under heating which contributed to the creation of more isolated graphene sheets and voids. The enhanced specific surface area and pore size of CoS@GN provided sufficient contact area to ensconce the surface chemical reaction and larger open channels for reactants to access the active catalytic centers. The XPS wide-scan spectra in Fig. 4D demonstrated the presence of Co, N, C, O elements in ZIF-67@GN [18]. For Co$_3$S$_4$@GN, the peak of N became negligible while an obvious signal of S appeared, suggesting the successful ligand displacement. The O peak tended to much weaker after heating as a result of the elimination of O-containing groups on graphene.

The core-level XPS spectra for C, Co and S elements were recorded to investigate the changes in chemical composition of obtained samples. In the C 1 s spectra (Fig. 5A), the intensity of the C–O/C−N peak at 285.5 eV of ZIF-67@GN decreased while the intensities of the C−C peak at 284.1 eV and C=O/C=N peak 288.1 eV increased under solvothermal treatment, indicating the release of 2-MIM and partial reduction or dehydration of GO [27]. For CoS@GN, both C–O and C=O peaks became weaker, suggesting most O-containing groups on graphene nanosheets were removed by 600 °C calcination. In Fig. 5B, the high-resolution Co 2p XPS spectrum of ZIF-67@GN was deconvoluted into only one spin-orbit doublet for Co(II), which was located at 780.7 eV (Co 2p$_{3/2}$) and 796.6 eV (Co 2p$_{1/2}$), respectively. Meanwhile, two broad peaks at 801.8 and 784.5 eV were assigned to the shakeup satellites. When it came to Co$_3$S$_4$@GN, a new doublet for Co(III) was observed at 778.3 eV (Co 2p$_{3/2}$) and 793.2 eV (Co 2p$_{1/2}$). The values of the binding energy of Co 2p$_{3/2}$, Co 2p$_{1/2}$, and two satellites were in good agreement with the reported characteristic peaks of Co$_3$S$_4$ [16]. For CoS@GN, the peak intensity of Co(II) increased markedly compared to that for Co$_3$S$_4$@GN, further confirming the conversion of Co$_3$S$_4$ into CoS. The weak peak of Co(III) was attributed to the remaining Co$_3$S$_4$ phase, which was not obvious in the XRD patterns. Sulfur species were

determined from the high-resolution XPS S 2p spectrum (Fig. 5C). The asymmetric peak observed at the lower binding energy could be fitted into two peaks at 162. 1 eV (S 2p$_{3/2}$) and 163.2 eV (S 2p$_{1/2}$) corresponding to the S^{2-} state in Co$_3$S$_4$ or CoS. The symmetric peak observed at the higher binding energy of 168.4 eV suggested the existence of S^{4+} species such as sulfite produced from the reaction between O-containing groups in GO with TAA-derived S, which were largely eliminated by thermal annealing [36].

3.2. Catalytic performance

The catalytic activity of as-prepared catalysts was evaluated by activating PMS to degrade BPA. As shown in Fig. 6A, nearly no BPA degradation was noticed when PMS alone was present, suggesting that the generation of oxidizing radicals from PMS barely occurred without catalysts. Meanwhile, only 20.39% of BPA adsorption was achieved by the use of CoS@GN-60 without addition of PMS. In contrast, the BPA concentration rapidly decreased when CoS@GN and PMS were combined, and over 92% of BPA was degraded within 8 min. To identify the possible contribution of the leachate in a homogeneous catalytic way, the filtrate collected from a suspension of CoS@GN-60 after being stirred for 8 min was used to catalyze the degradation of BPA. Almost no change in the BPA concentration was found. Meanwhile, 0.52 mg/L of Co leaching was detected by ICP after 8 min reaction in the CoS@GN-60/PMS/BPA system. The potential contribution of these dissolved Co ions to the catalytic reaction was also limited (< 5%), manifesting the BPA degradation by CoS@GN-60 followed a heterogeneous catalytic route. Impressively, the degradation process was significantly accelerated when increasing the graphene content in CoS@GN from 10 mg to 60 mg. For CoS@GN-60, 90.00% and 97.10% of BPA were removed in a duration of only 4 and 8 min, respectively, with a kinetic rate constant (k) reaching 0.62 min^{-1}. In the case of degrading BPA with a comparable reaction condition, the k value of CoS@GN-60 was much higher than those of most previously reported catalysts by 1–2 orders of magnitude (Table 1). Fig. 6B showed the critical role of thermal annealing in enhancing the catalytic efficiency. According to XRD results, the 600 °C heating converted Co$_3$S$_4$ to CoS in which Co existed as Co(II). These Co(II) could function as active centers to produce reactive radicals through the establishment of Co^{2+}-to-HSO$_5$-electron transfer [28]. As a result, the degradation processes of BPA by Co$_3$S$_4$ and Co$_3$S$_4$@GN-60 were substantially expedited after calcination. Meanwhile, the catalytic activities of Co$_3$S$_4$ and CoS both increased after being anchored on graphene nanosheets. The pure reduced graphene oxides (RGO) obtained from solvothermal reaction or further thermal treatment failed to induce obvious BPA degradation under the present condition, which excluded the contribution of metal-free
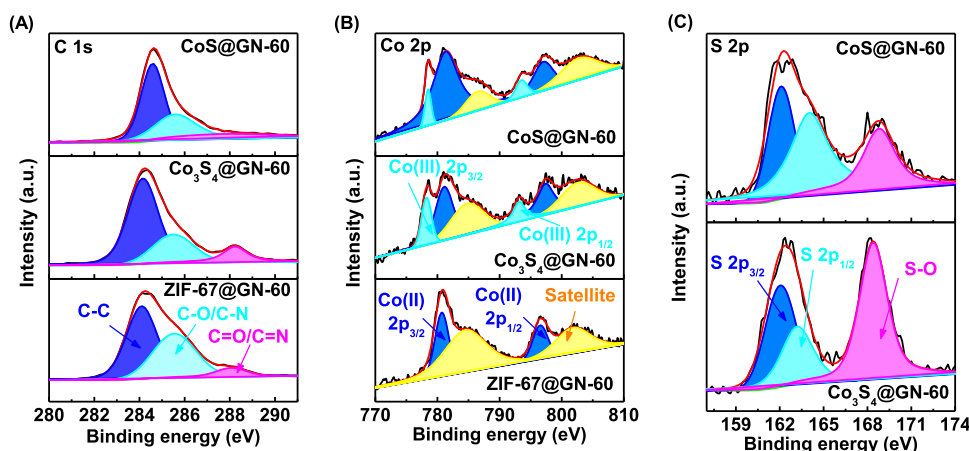

Fig. 5. Core-level XPS spectra of (A) C, (B) Co and (C) S elements in ZIF-67@GN-60, Co$_3$S$_4$@GN-60 and CoS@GN-60 samples.
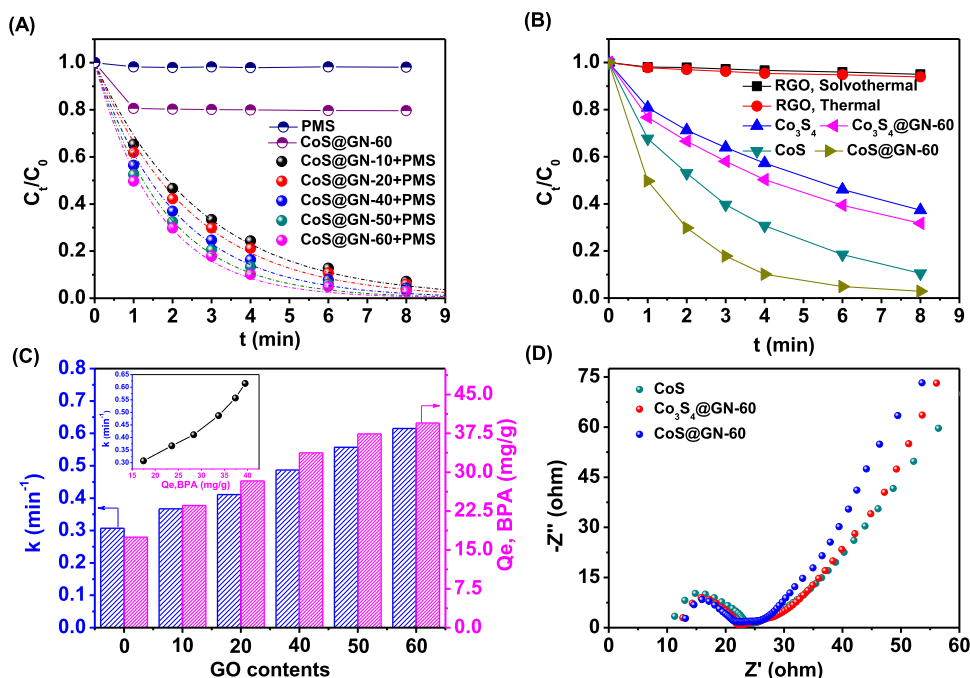
Fig. 6. (A) Removal efficiency of BPA in different reaction systems. The dotted lines were the fitting curves of the first-order kinetic equation. (B) Effect of thermal annealing on BPA degradation. (C) Dependence of first-order kinetic constants (k) and BPA adsorption amounts (Q_e) on the GO content in preparing CoS@GN catalysts. The inner image showed the relationship between k and Q_e. (D) Nyquist plots of CoS, Co_3S_4@GN-60 and CoS@GN-60 electrodes. Reaction conditions for (A, B): [catalysts] = 0.1 g/L, [PMS] = 0.1 g/L, [BPA] = 20 mg/L, pH_0 = 6.65.

catalysis of graphene. To understand the positive effect of graphene support, the adsorption capacities of CoS and CoS@GN for BPA (Q_e) were recorded as the indexes of the enrichment ability for targeted pollutant. The two-dimensional sp^2-hybridized carbon structure of graphene favored the adsorption of BPA through the strong π-π interaction [27]. As exhibited in Fig. 6C, the increase of graphene content from 0 to 60 mg increased the Q_e value from 17.45 mg/g to 39.49 mg/g. As a response, the first-order rate constant (k) for the BPA degradation increased from 0.31 min^{-1} to 0.62 min^{-1}. Plotting k against Q_e obtained a positively related curve, indicating the surface enrichment of BPA stimulated the degradation process. It was also noteworthy that the poor linear dependence between k and Q_e implied the participation of other factors in improving the catalytic activity. To probe the possible contribution of the conductivity of graphene, EIS measurements were carried out and the Nyquist plots of Co_3S_4@GN, CoS and CoS@GN-based electrodes were shown in Fig. 6D. A typical semicircle and a linear portion were visible, which could be ascribed to the charge-transfer resistance and mass-transfer resistance in the high-medium frequency region and the low frequency range, respectively [43]. The radius of the semicircle for CoS@GN was somewhat smaller than those of CoS and Co_3S_4@GN. It manifested that the charge transfer resistance of CoS was decreased after the introduction of graphene. Meanwhile, the thermal annealing swept most functional groups on graphene and

elevated the conductivity of Co_3S_4@GN, which accelerated the electron transfer to promote the catalytic activity of resulted CoS@GN.

Further investigations were performed to examine the effect of reaction parameters on BPA degradation by CoS@GN-60. Figure S3 A presented the degradation efficiency of BPA at varying BPA loads. The k value decreased from 1.39 min^{-1} to 0.32 min^{-1} when BPA concentration increased from 10 mg/L to 30 mg/L. The effect of PMS concentration on BPA removal was shown in Figure S3B. The addition of more PMS resulted in a faster BPA degradation. In the presence of 0.05 g/L PMS, BPA degradation slowed down obviously after 4 min as a result of the exhaustion of PMS. Further increasing PMS concentration from 0.10 to 0.15 g/L did not significantly increase the degradation efficiency, suggesting sufficient radicals were supplied by 0.10 g/L PMS. The impact of solution pH was examined in Figure S3C. The pH augment from 3.59 to 10.11 led to the enhanced BPA degradation. Compared to the neutral pH, the slightly lower k value in acid solution should originate from the stabilization effect of H^+ on HSO_5^- [7]. The significantly improved reaction rate at the alkaline side stemmed from the increasing amount of surface hydroxyls that accelerated the decomposition of PMS [44]. Overall, the CoS@GN-60/PMS system effectively degraded BPA over a wide range of pH, outperforming conventional Fenton or Fenton-like reactions. As shown in Figure S3D, the BPA degradation efficiency exhibited a positive dependence on the catalyst

Table 1
Comparison of the BPA degradation efficiency by CoS@GN-60 with those by previously reported catalysts through PMS activation.

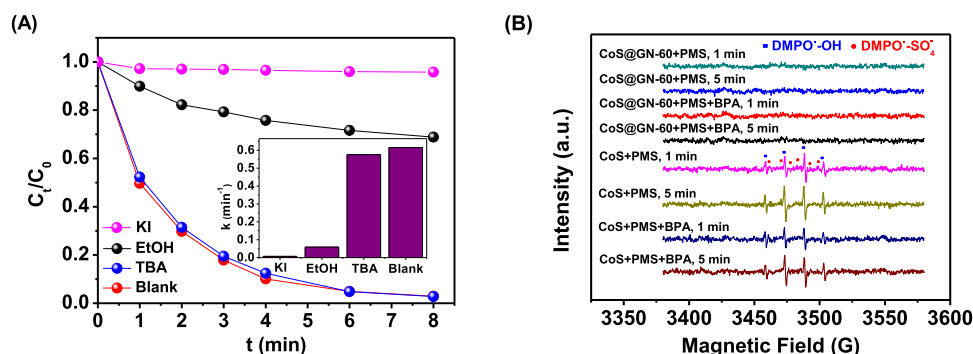| Catalyst	Dosage (g/L)	pH	C_{BPA} (mg/L)	C_{PMS} (g/L)	k (min^{-1})	Reference
MOF-derived N-doped Carbon Modified g-C_3N_4	–	7	20	0.152	0.00336	[37]
Polypyrrole-derived N-doped Carbon	0.1	7	20	0.494	0.036	[9]
Manganese/magnetite /graphene oxide	0.5	7	91.316	0.76	0.113	[38]
$Mn_{1.8}Fe_{1.2}O_4$ Nanosphere	0.1	7.5	10	0.2	0.10	[7]
Sulfur-doped Carbon Nitride	0.3	7	50	0.3	0.0083	[39]
$Fe_xCo_{3-x}O_4$ Nanocage	0.1	6	20	0.2	0.049	[11]
Graphene Encapsulated Fe_xCo_y Nanocage	0.1	6	20	0.2	0.132	[40]
Pd/g-C_3N_4	0.1	7	20	0.152	0.038	[41]
Dipicolinic Acid-functionalized Hematite	0.5	7	15	1	0.039	[42]
$Fe_xMn_{6-x}Co_4-N@C$	0.1	6	20	0.2	0.48	[8]
CoS@GN	0.1	6.7	20	0.1	0.62	This Work

Fig. 7. (A) Effect of radical scavengers on BPA degradation in the CoS@GN-60/PMS system. Reaction conditions: [catalysts] = 0.1 g/L, [PMS] = 0.1 g/L, [BPA] = 20 mg/L, [scavenger] = 0.2 mol/L, pH_0 = 6.65. (B) EPR spectra in PMS activation under different conditions.

dosage. When the dosage increased from 0.05 g/L to 0.15 g/L, the k value increased from 0.31 min^{-1} to 0.82 min^{-1}. This was attributed to the fact that increasing active sites derived from the higher catalyst dose facilitated the generation of more radicals from PMS.

3.3. Identification of surface-bound reactive radicals and catalytic mechanism

Two reactive oxygen species including $\cdot OH$ and $SO_4^{\cdot-}$ are commonly considered as the possible radicals in the Co-PMS catalytic system. To identify the radical species involved in the BPA degradation, quenching experiments were conducted by using ethanol (EtOH) and tert-butyl alcohol (TBA). EtOH with α-H is an excellent radical scavenger for both $\cdot OH$ (k = (1.2–2.8) × 10^9 $M^{-1}s^{-1}$) and $SO_4^{\cdot-}$ (k = (1.6–7.7) × 10^7 $M^{-1}s^{-1}$), whereas TBA without α-H is only effective for $\cdot OH$ (k= (3.8–7.6) × 10^8 $M^{-1}s^{-1}$) but not for $SO_4^{\cdot-}$ (k = (4.0–9.1) × 10^5 $M^{-1}s^{-1}$) [13]. Fig. 7A depicts the inhibition effect of the two quenchers on BPA degradation in the CoS@GN-60/PMS system. The addition of TBA had little influence on the elimination of BPA, which meant that the contribution of $\cdot OH$ to the BPA decomposition was ruled out. Conversely, the introduction of EtOH significantly depressed the removal of BPA, which implied that the radicals generated in the system were mostly quenched. Therefore, $SO_4^{\cdot-}$ was considered as the dominant radical species responsible for BPA degradation. Moreover, to determine the existence of surface-confined radicals, KI was used as another quencher because KI could react with surface-bound radicals. The addition of KI almost completely depressed the oxidation of BPA, suggesting the surface-bound $SO_4^{\cdot-}$ played the dominant role in the catalytic process. The electron paramagnetic resonance (EPR)/DMPO tests were performed to further confirm the involved radicals. As shown in Fig. 7B, characteristic signals for both DMPO- $SO_4^{\cdot-}$ and DMPO-$\cdot OH$ adducts were observed for pure CoS, which was consistent with previous reports using $Fe_xCo_{3-x}O_4$ and $Mn_{1.8}Fe_{1.2}O_4$ as PMS activators [7,11]. The $\cdot OH$ was produced by the reaction of $SO_4^{\cdot-}$ with H_2O/OH-. The time-dependent enhancement of both signals from 1 min to 5 min indicated the continuous generation of radicals. In the presence of BPA, the signal intensities of both DMPO $\cdot-OH$ and DMPO- $SO_4^{\cdot-}$ decreased substantially compared with the control groups without BPA, suggesting that both $\cdot OH$ and $SO_4^{\cdot-}$ were able to react with BPA. However, in the case of CoS@GN-60, the signs of DMPO-$SO_4^{\cdot-}$ and DMPO-$\cdot OH$ adducts turned silent in the EPR spectra of CoS@GN-60/PMS and CoS@GN-60/PMS/BPA systems at either 1 or 5 min. This result confirmed that the radicals were immediately confined on the catalyst surface once produced, and thus exhibited negligible EPR response. The contrary observations of pure CoS and CoS@GN-60 was undoubtedly originated from the structural differentiation associated with the graphene support. Wang et al. found that the surface-bound $SO_4^{\cdot-}$ rather than free $SO_4^{\cdot-}$ played a dominant role in the BPA oxidation by an N-doped RGO [27]. To probe the driving force for radical confinement, the surface chemistry of CoS@GN-60 was researched by

potentiometric titration and the pH-dependent apparent net surface charge (σ_0) was depicted in SI Figure S4. Note that σ_0 means the net amount of H^+ or OH- consumed by the catalyst sample through protonation/deprotonation during titration [45]. The pH_{pzc} of CoS@GN-60 was determined as 7.90. The catalyst surface carried positive charges at solution pH < 7.90, which covered the work pH window ranging from 6.65 to 3.49 (SI Figure S5). Therefore, the radical, which was more supposed to be the negative $SO_4^{\cdot-}$ rather than uncharged $\cdot OH$, could be bound on the surface of CoS@GN-60 through electrostatic attraction. Based on the above observations, we proposed the process mechanism as Fig. 8. First, PMS was activated by CoS to produce vast $SO_4^{\cdot-}$. Second, for the pristine CoS with poor efficiencies for BPA enrichment and electron transfer, the $SO_4^{\cdot-}$ tended to accumulate then diffuse out of catalyst surface after saturation, as well as be consumed by H_2O/OH- as a side reaction to generate $\cdot OH$. The released $SO_4^{\cdot-}$ and $\cdot OH$ were readily trapped by DMPO in solution and emitted sound EPR signals. For CoS@GN-60, the presence of graphene support provided adsorption domains for BPA and high-speed channels for electron flow. Unlike $\cdot OH$, $SO_4^{\cdot-}$ preferred to degrade BPA molecule in the way of charge transfer [46]. So, the $SO_4^{\cdot-}$ once produced was bound onto catalyst surface through electrostatic force and then rapidly seized the electrons from absorbed BPA with graphene as the conductor. Consequently, no redundant $SO_4^{\cdot-}$ was released into the bulk solution to combine with DMPO. Meanwhile, the generation of $\cdot OH$ by the reaction of $SO_4^{\cdot-}$ with H_2O/OH- was limited. The complete in-situ surface reaction of $SO_4^{\cdot-}$ and BPA contributed to the ultrahigh degradation rate.

For a better insight into the catalytic mechanism, a series of characterizations on the fresh and used catalysts were carried out. The high-resolution XPS spectra of CoS@GN-60 before and after reactions were used to clarify the structural change and the redox cycling of Co species
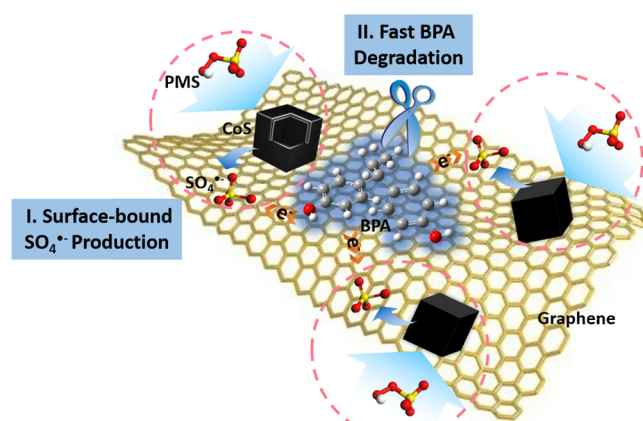

Fig. 8. Schematic diagram of mechanisms for surface-bound $SO_4^{\cdot-}$ generation and electron transfer through graphene support for in-situ BPA degradation on CoS@GN-60 surface.
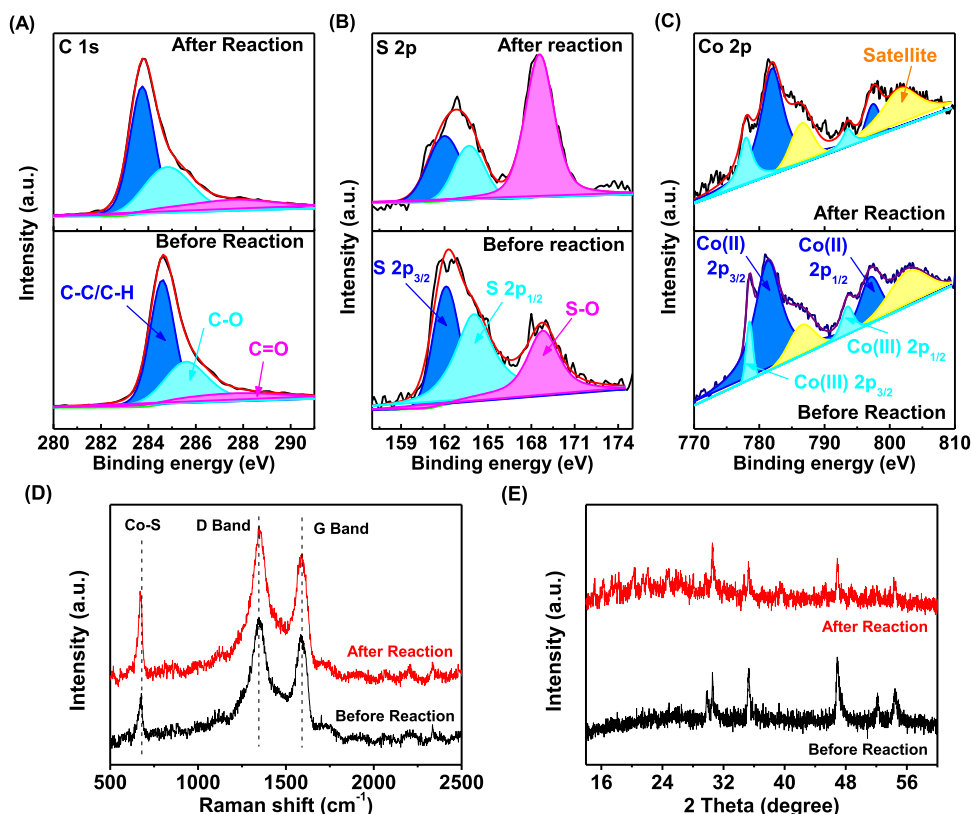
Fig. 9. Core-level XPS spectra of (A) C, (B) S and (C) Co elements in fresh and used CoS@GN-60 samples. (D) Raman spectra and (E) XRD patterns of CoS@GN-60 samples before and after reactions.

during the reaction process. According to the C 1S and S 2p core-level XPS spectra (Fig. 9A, B), more oxygen-containing species including C–O, C=O and S–O groups appeared on graphene plane after reaction, which was assigned to the inescapable oxidation of graphene by $SO_4^{\cdot -}$ during electron transport. When the catalysis ended, the relative intensity of Co(II) peak was declined, whereas the Co(III) peak was strengthened (Fig. 9C). So, a part of Co(II) was converted into Co(III) during the activation of PMS. The Raman spectra were also used to investigate the structural change of catalysts (Fig. 9D). The intensity ratio of D and G bands (I_D/I_G) increased from 1.12 to 1.17 after reaction, suggesting the sp^2 carbon framework was somewhat disturbed due to the oxidation of graphene. In the XDR patterns (Fig. 9E), the small peaks at 2θ values of 16–28° were ascribed to the Co(III)-containing Co_3S_4, which was consistent to the above XPS results. However, the

overall structure change was minimal, implying the good stability of CoS@GN-60.

The density functional theory (DFT) calculation was applied to further uncover the PMS activation process on CoS@GN-60. The (100) lattice plane of CoS crystal was used as the representative face. The relaxed atomic structures of a PMS molecule adsorption on CoS before and after configuration optimization were showed in SI Figure S6 and Fig. 10, respectively. The PMS was directly dissociated into OH and SO_4 fragments after being placed on CoS. Meanwhile, the SO_4 group was chemically connected to the catalyst surface through a covalent bond, i.e., an O atom bonding with a Co atom below, which benefitted the electron donation from Co(II) to SO_4 to produce $SO_4^{\cdot -}$. The adsorption energy (E_{ads}) of PMS on the CoS model was determined by $E_{ads} = E_{CoS+PMS} - E_{PMS} - E_{CoS}$, where E_{CoS+PM}, E_{PMS} and E_{CoS} were the total
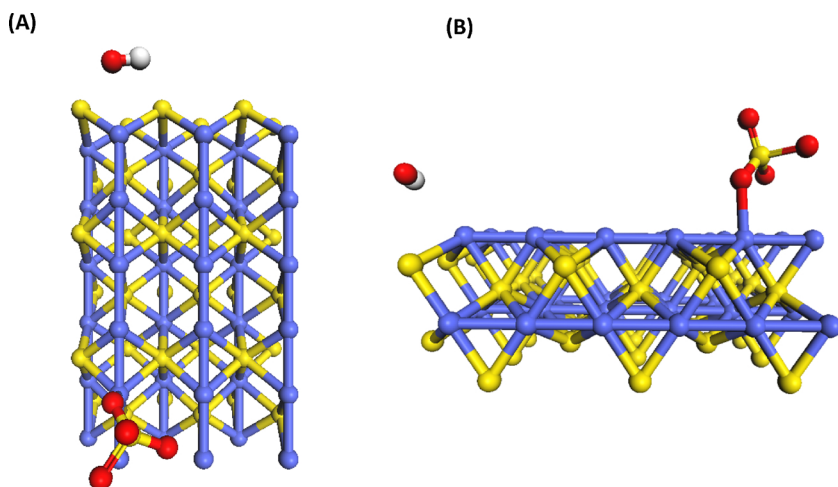

Fig. 10. Perspective projection images (A. top view, B. side view) of PMS adsorption configuration on CoS (100) crystal face after geometry optimization by DFT calculation. The red, yellow, white and blue spheres were O, S, H and Co atoms, respectively (For interpretation of the references to colour in this figure legend, the reader is referred to the web version of this article).
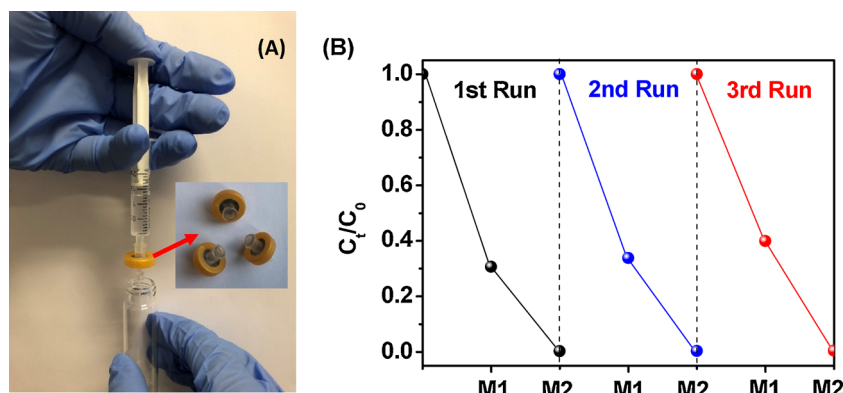
Fig. 11. (A) Photograph of the CoS@GN-60-coated membrane reactor. (B) BPA degradation using a two-grade CoS@GN-60-coated membrane reactor system in consecutive 3 cycles. Reaction conditions: Volume = 2 mL, flow rate = 1 mL/min, [PMS] = 0.1 g/L, [BPA] = 10 mg/L, pH_0 = 6.65.

energies of the CoS surface with PMS adsorption, an isolated PMS molecule and the CoS surface, respectively. The adsorption of PMS on CoS surface was quite strong with E_{ads} being -7.56 eV, the absolute value of which was higher than those of previous reports using MnN_4 and N-doped nanocarbon for PMS activation [8,47]. The direct dissociation of PMS on catalyst surface and high absolute value of E_{ads} suggested the excellent activity of CoS@GN-60 in yielding $SO_4^{\cdot-}$ to degrade BPA.

These results indicated that the activation of PMS occurred on the catalyst surface. Co(II) donated electrons to PMS and thus initiated its decomposition (Eq. (3)). The produced Co(III) was then reduced by HSO_5^- to complete the redox cycle (Eq. (4)), which made the catalytic action of CoS@GN-60 work continuously. In this process, $\cdot$OH was not generated as the surface-bound $SO_4^{\cdot-}$ was immediately consumed to form SO_4^{2-} with the electrons from adsorbed BPA transferred by the underlying graphene (Eq. (5)). Afterwards, BPA was decomposed into various intermediates and finally mineralized.

$$Co(II)+HSO_5^- \to Co(III)+SO_4^{\cdot-}+OH^- \qquad (3)$$

$$Co(III)+HSO_5^- \to Co(II)+SO_5^{\cdot-} + H^+ \qquad (4)$$

$$SO_4^{\cdot-}+BPA \to intermediates + SO_4^{2-} \to CO_2 + H_2O+SO_4^{2-} \qquad (5)$$

3.4. TOC removal and possible degradation pathway of BPA

The TOC analysis was used to evaluate the mineralization of BPA (SI Figure S7). It was found that 40.64% of BPA was mineralized within 8 min, confirming that BPA was not only degraded to small organic compounds, but even mineralized to CO_2. The main aromatic intermediates from BPA degradation were identified as phenol, 4-isopropenylphenol and 3,5-bis(1,1-dimethyl(ethyl)) phenol by the GC–MS (SI Figures S8). Based on the experimental results and previous studies [9,11], the possible degradation pathway of BPA induced by the activation of PMS over CoS@GN-60 was proposed in SI Figure S9. First, the quaternary carbon atom located in the center of BPA molecule was attacked by $SO_4^{\cdot-}$ and thus phenoxyl (PhO) and isopropenylphenol (IPP) radicals were produced through the β-scission (C-C), which were immediately transformed to the phenol and 4-isopropenylphenol, respectively. Meanwhile, PhO and IPP radicals were also transferred to the 4,4′-((5-hydroxy-1,3-phenylene)bis(propane-2,2-diyl))diphenol through addition reaction, which was then decomposed to generate the 3,5-bis(1,1-dimethyl(ethyl)) phenol. Afterwards, numbers of aromatic intermediates were formed through the dehydration, oxidative skeletal rearrangement, etc. Finally, ring-opening products including maleic, oxalic, formic, acetic and malonic acids were formed, which were ultimately mineralized into CO_2 and H_2O.

3.5. Construction of CoS@GN-60-Coated membrane and reusability

The nanoscale catalysts were difficult to be recovered from water after use, so energy-intensive and time-consuming post-processes such as the high-speed centrifugation were required to separate the solid catalysts, which impeded the practical application of nanomaterials. Herein, the suspension with well-dispersed CoS@GN-60 nanocomposites was filtrated through an inert polytetrafluoroethylene (PTFE) membrane to construct a simple CoS@GN-60-coated membrane reactor (Fig. 11A). The CoS@GN-60 coating could purify the flowing BPA-containing water while the underlying PTFE film prevented the catalyst loss without any post-separation. In a facile procedure, the BPA solution was filtrated through the active membrane with an injection syringe forcibly. To improve the degradation efficiency, two membrane reactors were connected for constructing a two-grade reactor system. The feasibility and reusability of this system was investigated as Fig. 11B. In the 1 st run, the BPA concentration was decreased by 69.35% with the first membrane reactor (M1), and after the second filtration (M2), BPA was almost completely removed. Moreover, the reactor system worked with similar high efficiency in subsequent two runs, suggesting the good reusability of CoS@GN-60 and system robustness.

4. Conclusion

This work presented the successful fabrication of novel graphene-supported cobalt sulfide nanocomposites via a facile MOF-templated ligand exchange strategy and first demonstrated their feasibility in SR-AOP for environmental application. In combination with subsequent calcination, highly-dispersed CoS nanocrystals were obtained from phase transformation and uniformly anchored on graphene nanosheets. Benefiting from the adsorptive and conductive graphene support as well as abundant Co(II) species in CoS, the nanocatalyst showed a superior catalytic activity in activating PMS for BPA degradation. The kinetic constant outperformed those of most previous reports by 1–2 orders of magnitude. Further investigations including the effect of reaction parameters and identification of intermediates as well as mineralization proved that BPA could be effectively degraded in a broad pH range with reasonable catalyst and oxidant dosages. Quenching tests and EPR detections revealed the critical role of graphene in the generation of surface-bound $SO_4^{\cdot-}$. Catalyst characterizations and the DFT simulation suggested the excellent efficiency of CoS@GN-60 in PMS activation with Co(II) as active centers. A simple CoS@GN-60-coated membrane reactor was constructed to avoid catalyst loss and worked well in consecutive 3 cycles, implying the satisfactory reusability of the as-prepared catalyst and system robustness. Overall, this work provided a novel family of Co-based nanocatalysts to generate surface-bound radicals for the rapid degradation of BPA, and paved the way for the application of other metal-organic frameworks as precursors to

construct metal sulfides as promising candidates for EDCs-contaminated water remediation by the aforementioned advanced oxidation process.

Acknowledgements

Appendix A. Supplementary data

Supplementary material related to this article can be found, in the online version, at doi:https://doi.org/10.1016/j.apcatb.2018.09.088.

References

[1] U. Rajamani, A.R. Gross, C. Ocampo, A.M. Andres, R.A. Gottlieb, D. Sareen, Nat. Commun. 8 (2017) 219.
[2] J. Moreman, A. Takesono, M. Trznadel, M.J. Winter, A. Perry, M.E. Wood, N.J. Rogers, T. Kudoh, C.R. Tyler, Environ. Sci. Technol. 52 (2018) 6656–6665.
[3] J.K. Thomas, O. Birceanu, B. Sadoul, M.M. Vijayan, Environ. Sci. Technol. 52 (2018) 7951–7961.
[4] S.B. Hammouda, F. Zhao, Z. Safaei, D.L. Ramasamy, B. Doshi, M. Sillanpää, Appl. Catal. B: Environ. 233 (2018) 99–111.
[5] X. Chen, W.D. Oh, Z.T. Hu, Y.M. Sun, R.D. Webster, S.Z. Li, T.T. Lim, Appl. Catal. B: Environ. 225 (2018) 243–257.
[6] L. Tang, Y. Liu, J. Wang, G. Zeng, Y. Deng, H. Dong, H. Feng, J. Wang, B. Peng, Appl. Catal. B: Environ. 231 (2018) 1–10.
[7] G.X. Huang, C.Y. Wang, C.W. Yang, P.C. Guo, H.Q. Yu, Environ. Sci. Technol. 51 (2017) 12611–12618.
[8] X. Li, Z. Ao, J. Liu, H. Sun, A.I. Rykov, J. Wang, ACS Nano 10 (2016) 11532–11540.
[9] P. Hu, H. Su, Z. Chen, C. Yu, Q. Li, B. Zhou, P.J.J. Alvarez, M. Long, Environ. Sci. Technol. 51 (2017) 11288–11296.
[10] X. Duan, C. Su, J. Miao, Y. Zhong, Z. Shao, S. Wang, H. Sun, Appl. Catal. B: Environ. 220 (2018) 626–634.
[11] X. Li, Z. Wang, B. Zhang, A.I. Rykov, M.A. Ahmed, J. Wang, Appl. Catal. B: Environ. 181 (2016) 788–799.
[12] S.B. Hammouda, F. Zhao, Z. Safaei, V. Srivastava, D. Lakshmi Ramasamy, S. Iftekhar, S. kalliola, M. Sillanpää, Appl. Catal. B: Environ. 215 (2017) 60–73.
[13] T. Zeng, X. Zhang, S. Wang, H. Niu, Y. Cai, Environ. Sci. Technol. 49 (2015) 2350–2357.
[14] Z. Huang, H. Bao, Y. Yao, W. Lu, W. Chen, Appl. Catal. B: Environ. 154–155 (2014) 36–43.
[15] Q. Zhou, L. Liu, Z. Huang, L. Yi, X. Wang, G. Cao, J. Mater. Chem. A Mater. Energy Sustain. 4 (2016) 5505–5516.
[16] Y. Guo, J. Tang, H. Qian, Z. Wang, Y. Yamauchi, Chem. Mater. 29 (2017) 5566–5573.
[17] D. Ghosh, C.K. Das, ACS Appl. Mater. Interfaces 7 (2015) 1122–1131.
[18] T. Chen, Z. Zhang, B. Cheng, R. Chen, Y. Hu, L. Ma, G. Zhu, J. Liu, Z. Jin, J. Am. Chem. Soc. 139 (2017) 12710–12715.
[19] Y. Ma, Y. Ma, D. Bresser, Y. Ji, D. Geiger, U. Kaiser, C. Streb, A. Varzi, S. Passerini, ACS Nano 12 (2018) 7220–7231.
[20] S. Kong, Z. Jin, H. Liu, Y. Wang, J. Phys. Chem. C 118 (2014) 25355–25364.
[21] Y. Yao, Y. Zhu, J. Huang, J. Shen, C. Li, Electrochim. Acta 271 (2018) 242–251.
[22] S. Dou, C.L. Dong, Z. Hu, Y.C. Huang, J.L. Chen, L. Tao, D. Yan, D. Chen, S. Shen, S. Chou, S. Wang, Adv. Funct. Mater. 27 (2017) 1702546–1702554.
[23] E.J. Carrington, C.A. McAnally, A.J. Fletcher, S.P. Thompson, M. Warren, L. Brammer, Nat. Chem. 9 (2017) 882–889.
[24] Z.F. Huang, J. Song, K. Li, M. Tahir, Y.T. Wang, L. Pan, L. Wang, X. Zhang, J.J. Zou, J. Am. Chem. Soc. 138 (2016) 1359–1365.
[25] Y. Zhao, Q. Pang, Y. Meng, Y. Gao, C. Wang, B. Liu, Y. Wei, F. Du, G. Chen, Chem. -Eur. J. 23 (2017) 13150–13157.
[26] Y. Gu, Y. Xu, Y. Wang, ACS Appl. Mater. Interfaces 5 (2013) 801–806.
[27] X. Wang, Y. Qin, L. Zhu, H. Tang, Environ. Sci. Technol. 49 (2015) 6855–6864.
[28] C. Wang, P. Shi, X. Cai, Q. Xu, X. Zhou, X. Zhou, D. Yang, J. Fan, Y. Min, H. Ge, W. Yao, J. Phys. Chem. C 120 (2015) 336–344.
[29] K.Y.A. Lin, W.D. Lee, Chem. Eng. J. 284 (2016) 1017–1027.
[30] J.H. Joshi, D.K. Kanchan, M.J. Joshi, H.O. Jethva, K.D. Parikh, Mater. Res. Bull. 93 (2017) 63–73.
[31] Y. Wang, J. Wu, Y. Tang, X. Lu, C. Yang, M. Qin, F. Huang, X. Li, X. Zhang, ACS Appl. Mater. Interfaces 4 (2012) 4246–4250.
[32] P. Sennu, M. Christy, V. Aravindan, Y.G. Lee, K.S. Nahm, Y.S. Lee, Chem. Mater. 27 (2015) 5726–5735.
[33] J. Wang, B. Chen, B. Xing, Environ. Sci. Technol. 50 (2016) 3798–3808.
[34] K.Y. Lin, H.A. Chang, Chemosphere 139 (2015) 624–631.
[35] H. Liu, P. Sun, M. Feng, H. Liu, S. Yang, L. Wang, Z. Wang, Appl. Catal. B: Environ. 187 (2016) 1–10.
[36] M. Chauhan, K.P. Reddy, C.S. Gopinath, S. Deka, ACS Catal. 7 (2017) 5871–5879.
[37] Y. Gong, X. Zhao, H. Zhang, B. Yang, K. Xiao, T. Guo, J. Zhang, H. Shao, Y. Wang, G. Yu, Appl. Catal. B: Environ. 233 (2018) 35–45.
[38] J. Du, J. Bao, Y. Liu, H. Ling, H. Zheng, S.H. Kim, D.D. Dionysiou, J. Hazard. Mater. 320 (2016) 150–159.
[39] K.Y.A. Lin, Z.Y. Zhang, Chem. Eng. J. 313 (2017) 1320–1327.
[40] X. Li, A.I. Rykov, B. Zhang, Y. Zhang, J. Wang, Catal. Sci. Technol. 6 (2016) 7486–7494.
[41] Y. Wang, D. Cao, M. Liu, X. Zhao, Catal. Commun. 102 (2017) 85–88.
[42] W.D. Oh, S.K. Lua, Z. Dong, T.T. Lim, J. Mater. Chem. A Mater. Energy Sustain. 2 (2014) 15836–15845.
[43] J. Hu, D. Chen, N. Li, Q. Xu, H. Li, J. He, J. Lu, Appl. Catal. B: Environ. 217 (2017) 224–231.
[44] C. Qi, X. Liu, J. Ma, C. Lin, X. Li, H. Zhang, Chemosphere 151 (2016) 280–288.
[45] B. Pan, F. Han, G. Nie, B. Wu, K. He, L. Lu, Environ. Sci. Technol. 48 (2014) 5101–5107.
[46] Z. Xu, C. Shan, B. Xie, Y. Liu, B. Pan, Appl. Catal. B: Environ. 200 (2017) 439–447.
[47] G. Wang, S. Chen, X. Quan, H. Yu, Y. Zhang, Carbon 115 (2017) 730–739.